catalysts

MDPI

Article

Modification of α-Fe_2O_3 Nanoparticles with Carbon Layer for Robust Photo-Fenton Catalytic Degradation of Methyl Orange

Muhammad Qasim [1,*], Mohamed A. Ghanem [2,*], Xuecheng Cao [1] and Xiaojie Li [1]

[1] Basic Department, Qilu Institute of Technology, Jinan 250200, China; xccao@sdau.edu.sa (X.C.); xjli@qlit.edu.cn (X.L.)
[2] Chemistry Department, College of Science, King Saud University, Riyadh 11451, Saudi Arabia
* Correspondence: qasim@qlit.edu.cn (M.Q.); mghanem@ksu.edu.sa (M.A.G.)

Abstract: The degradation of organic dyes poses a significant challenge in achieving sustainable environmental solutions, given their extensive usage across various industries. Iron oxide (Fe_2O_3) nanoparticles are studied as a reliable technique for remediating dye degradation. The objective of this research is to improve methods of nanomaterial-based environmental remediation. The solvothermal technique is used to synthesize carbon-modified Fe_2O_3 nanoparticles that exhibit the capability to modify their size morphology and increase reactivity, and stability for MO photodegradation. Their inherent qualities render them highly advantageous for biomedical applications, energy storage, environmental remediation, and catalysis. The mean crystallite size of the modified Fe_2O_3 nanoparticles is approximately 20 nm. These photocatalysts are tested for their ability to degrade methyl orange (MO) under Visible light radiation and in presence of hydrogen peroxide reagent. The optimal degradation efficiency (97%) is achieved with Fe_2O_3@C in the presence of H_2O_2 by meticulously controlling the pH, irradiation time, and photocatalyst dosage. The enhanced photocatalytic activity of the Fe_2O_3@C nanoparticles, compared to pure Fe_2O_3, is attributed to the conductive carbon layer, which significantly reduces electron-hole recombination rates. To summarize, Fe_2O_3@C nanoparticles not only offer a promising technique for the degradation of MO dye pollutants but also have an advantage for environmental remediation due to their increased stability and reactivity.

Keywords: Fe_2O_3 nanoparticles; visible light-dependent; photocatalytic degradation of MB; characterization

Citation: Qasim, M.; Ghanem, M.A.; Cao, X.; Li, X. Modification of α-Fe_2O_3 Nanoparticles with Carbon Layer for Robust Photo-Fenton Catalytic Degradation of Methyl Orange. *Catalysts* **2024**, *14*, 393. https://doi.org/10.3390/catal14060393

Academic Editor: Natalia Martsinovich

Received: 29 April 2024
Revised: 8 June 2024
Accepted: 12 June 2024
Published: 20 June 2024

1. Introduction

Methyl orange (MO) is categorized as an anionic or acidic dye since it is a water-soluble azo dye [1]. High amounts of this dye can be lethal in severe situations and cause symptoms including nausea and diarrhea when ingested or exposed to [1,2]. It is stable, resistant to biodegradation, and water-soluble, making it difficult to eliminate from water using conventional remedy techniques [3–5]. Three main strategies are usually used to remove dye pollution from effluents: chemical treatments, physical separation, or biological degradation [6]. However, the efficient techniques for eliminating organic substances from wastewater, specifically dyes, encompass ion exchange, adsorption, membrane filtration, coagulation-flocculation, advanced photo-oxidation processes, and aerobic-anaerobic digesting [6–10].

The advanced photo-oxidation process is the most efficient technique because it's low-cost, operates at low temperatures, and can convert organic pollutants into harmless substances like carbon dioxide (CO_2) and water (H_2O). Photocatalysis, a key component in these techniques, has consistently demonstrated remarkable efficacy in eliminating organic pigments [3]. Both electron–hole pairs are produced on the catalyst's surface when electrons in the valence band of the catalyst are promoted to the conduction band by exposure to ultraviolet or visible light [11]. Subsequently, these pairs of electrons and holes interact

with water molecules, resulting in the creation of hydroxide (•OH) free radicals [12]. These radicals are widely recognized for their ability to degrade dyes into harmless substances such as carbon dioxide and water [5].

A variety of catalysts have been employed for the degradation of organic dyes, such as Cu/Ni-doped nanostructures, Fe_2O_3 nanoparticles, polymeric hydrogel containing TiO_2 nanoparticles, Fe_2O_3/ZnO, Fe_2O_3/SiO_2, CeO_2/Ce_2S_3 composites, Ch-Pani/Fe_2O_3, C_3N_4/Fe_2O_3, polyaniline/SnO_2 nanospheres, Fe_2O_3/ZnTe, Fe_2O_3/Mn_3O_4, CuO/ZnO nanocomposites, and tellurium-based metal alloys [6,11–19]. Among these catalysts, hematite (Fe_2O_3) stands out for its remarkable qualities, which include resistance to corrosion, high efficiency, and non-toxicity [20].

In particular, the carbon coating Fe_2O_3 nanoparticles were found to reduce photocorrosion and degradation, enhancing stability and extending its lifespan in photocatalytic applications [6–11]. The significance of a carbon layer enables rapid electron transfer and reduces electron–hole recombination, enhancing photocatalytic activity [8,9]. Without the carbon layer, Fe_2O_3 nanoparticles have higher recombination rates, lowering their photocatalytic efficiency, especially in harsh conditions. In addition, the carbon layer absorbs a broader range of light, allowing the composite to utilize more of the visible spectrum compared to pure Fe_2O_3 nanoparticles. Furthermore, the carbon layer increases the number of active sites on Fe_2O_3 nanoparticles, and improves the electron mobility and effective charge carrier generation as compared to pure Fe_2O_3 nanoparticles, leading to more efficient photocatalytic reactions [8,9]. Moreover, hydrogen peroxide (H_2O_2) reagent can be added to the Fe_2O_3-based photocatalytic reaction to further increase the production of hydroxide free radicals (•OH) via the Fenton reaction [21–24], which enrich the organic compound oxidation process via the heterogeneous photo-Fenton–catalytic oxidation reaction [21–24]. These enhancements highlight the importance and novelty of using carbon-covered Fe_2O_3 in Fenton photocatalytic degradation of organic compounds.

Electrospinning, co-precipitation, combustion, hydrothermal, thermal decomposition, and microwave/ultrasound processes have all been utilized in the production of Fe_2O_3 nanoparticles [3,25–29].

However, these techniques frequently call for pricey supplies or complex equipment. To overcome these drawbacks and benefit from simplicity, low heat requirements, and affordability, the solvothermal/hydrothermal approach was chosen to synthesize the catalyst nanoparticles. In this work, both pure Fe_2O_3 and carbon-modified Fe_2O_3 (Fe_2O_3@C) nanoparticles were prepared by a simple solvothermal/hydrothermal method. The synthesized nanoparticles with a carbon layer have effectively enhanced the photo-degradation of MO dye. The investigation also examined several variables that affect the photo-degradation process, including the dosage, duration, pH value, addition of H_2O_2 reagent and concentration of the dye.

2. Results and Discussion

2.1. Structural Analysis

In this section, the structural properties of pure α-Fe_2O_3 and carbon-modified Fe_2O_3@C nanoparticles synthesized through the solvothermal method were studied thoroughly. Figure 1a shows the XRD patterns and crystal structure of the pure Fe_2O_3 and Fe_2O_3@C catalysts. As illustrated in Figure 1a, the main diffraction peaks arise at 2θ = 24.19°, 33.21°, 35.70°, 40.94°, 49.55°, 54.15°, 62.56°, and 64.14°, etc., can be assigned to the (012), (104), (110), (113), (024), (116), (018), (214), and (300) crystal planes, respectively [3,27]. The crystal structure of the synthesized photocatalyst is rhombohedral, and the obtained peaks are well-matched with the hematite α-Fe_2O_3 card JCPDS 01-084-0307. Using the Scherrer equation, the average crystallite size of the pure Fe_2O_3 and Fe_2O_3@C photocatalysts was 20 and 50 nm, respectively. Similarly, the close relationship between the C layer is responsible for the contrasting peak intensity observed in Fe_2O_3@C and pure Fe_2O_3. Unfortunately, XRD lacks the sensitivity to gather data on the amorphous carbon structure, as its concentration is relatively low.

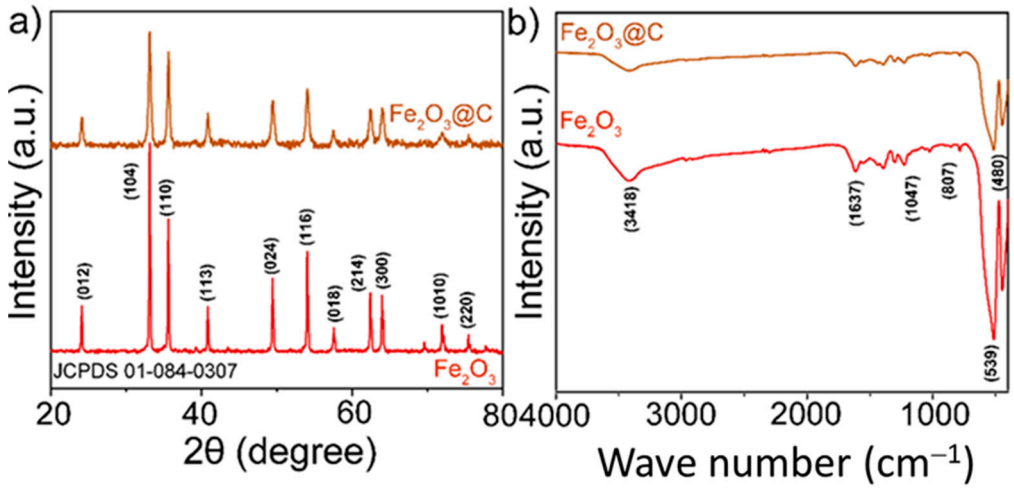

Figure 1. (**a**) XRD patterns of the pure Fe_2O_3 and carbon-modified Fe_2O_3/C nanoparticles, (**b**) corresponding FTIR analysis of pure Fe_2O_3 and carbon-modified Fe_2O_3/C nanoparticles.

Additionally, Figure 1b depicts the FTIR spectrum of the pure Fe_2O_3 and Fe_2O_3@C nanoparticles, which indicates that the absorption band at a high wavenumber region is due to OH stretching, and at a lower wavenumber because of FeO lattice vibration. The OH stretching (υOH) and HOH bending (δOH) vibrational bands are present in all samples at 3423–3444 cm^{-1} and 1637 cm^{-1}, respectively [30]. The obtained FTIR spectrum of pure Fe_2O_3 is very consistent with that reported in the literature [31]. The broad absorption band observed at 3418 cm^{-1} was ascribed to the elongation of "loosely bound water" adsorbed on the surface of goethite and hydroxyl groups [20]. Moreover, the prominent absorption peaks observed at 480 cm^{-1} and 539 cm^{-1} correspond to the stretching vibrations of the Fe-O bond, which are distinctive properties of this element [20].

2.2. Morphological Analysis

Figure 2 shows the SEM, TEM, and HRTEM analysis of pure Fe_2O_3 and Fe_2O_3@C nanoparticles. The SEM images in Figure 2a,d show the confirmation of surface morphology of the pure Fe_2O_3 and Fe_2O_3@C nanoparticles, respectively. Both catalysts exhibit irregular nanoparticle morphology and are randomly assigned to Fe_2O_3, depending on the contrast difference. Next, the TEM analysis of pure Fe_2O_3 and Fe_2O_3@C nanoparticles are shown in Figure 2b, and Figure 2e, respectively. The results validate the presence of nanoparticle structure for both pure Fe_2O_3 and Fe_2O_3@C catalysts that exhibit spherical and irregular shapes, with an average diameter ranging from 20 nm to 50 nm, respectively. This understanding can be further verified by HRTEM analysis as shown in Figure 2c,f. The measured lattice spacing of 0.28 nm can be assigned to the Fe_2O_3 {104}, plane in both catalysts. However, the lattice fringes in the case of pure Fe_2O_3 are more visible and well-defined in contrast to Fe_2O_3@C nanoparticle suggesting the amorphous structure of the carbon-modified Fe_2O_3. Furthermore, to confirm the formation of an amorphous structure in the case of Fe_2O_3@C nanoparticles, the STEM analysis of both Fe_2O_3@C and pure Fe_2O_3 nanoparticles are shown in Figure 3 and Figure 4, respectively. A closer investigation indicates that the surface of the Fe_2O_3@C nanoparticle is covered by a thin carbon layer as shown in Figure 3b. In the interim, it was discovered that the encapsulating carbon layer comprised of amorphous carbon and measured around 3–4 nm in thickness on the Fe_2O_3 surface is the evidence of our previous findings [20]. For comparison purposes, the pure Fe_2O_3 nanoparticles without carbon layers have similar shapes with no carbon contrast as shown in Figure 4d. Furthermore, to confirm the presence of a conductive carbon layer around the Fe_2O_3 nanoparticles we synthesized similar shapes and sizes of Fe_2O_3 nanoparticles without a carbon layer. The content of C in Fe_2O_3@C was obtained with the help of elemental analysis. After careful measurement, we found that the weight percentage of C in the composite Fe_2O_3@C is higher (i.e., 1.95), as compared to pure Fe_2O_3

(i.e., 0.75). This analysis provides additional evidence that Fe_2O_3 is covered by a carbon layer. This result also supports our previous findings [20].

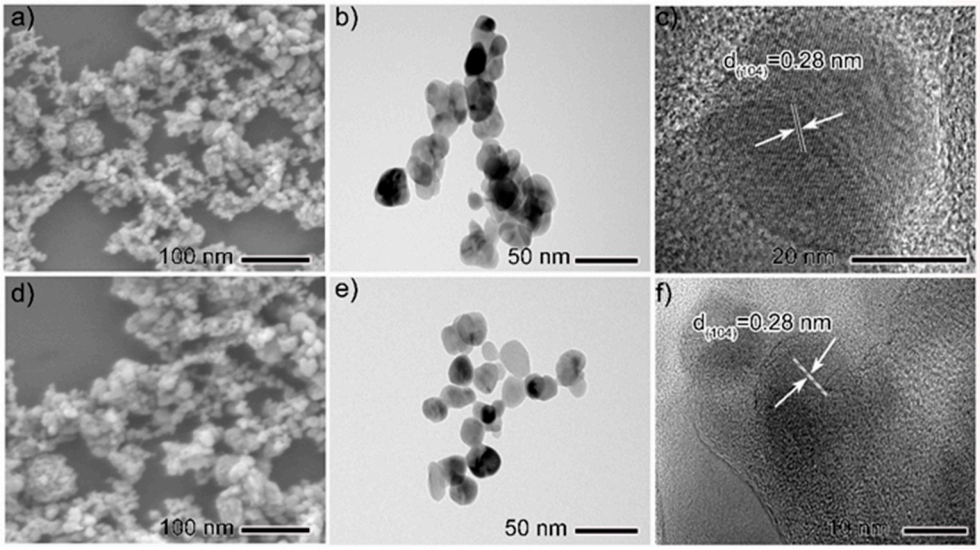

Figure 2. (**a**,**d**) SEM Images (**b**,**e**) TEM images, and (**c**,**f**) HRTEM images pure Fe_2O_3 and Fe_2O_3/C nanoparticles, respectively. The arrows show the lattice spacing.

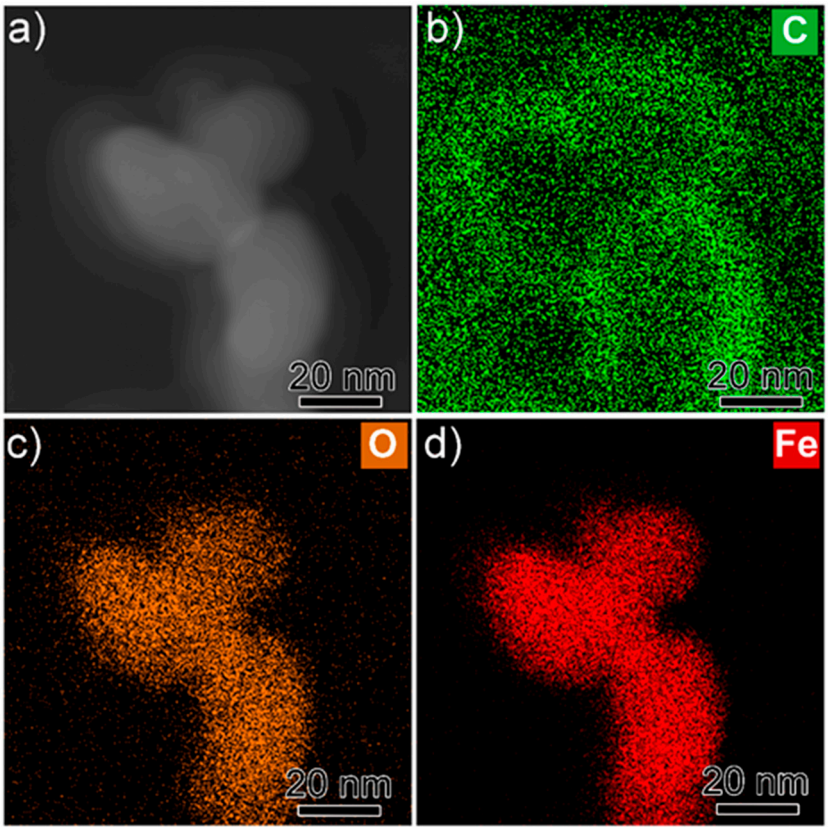

Figure 3. (**a**) STEM analysis of Fe_2O_3/C nanoparticles without carbon layer, and (**b**–**d**) corresponding elemental mapping analysis of Fe, O, and C, respectively.

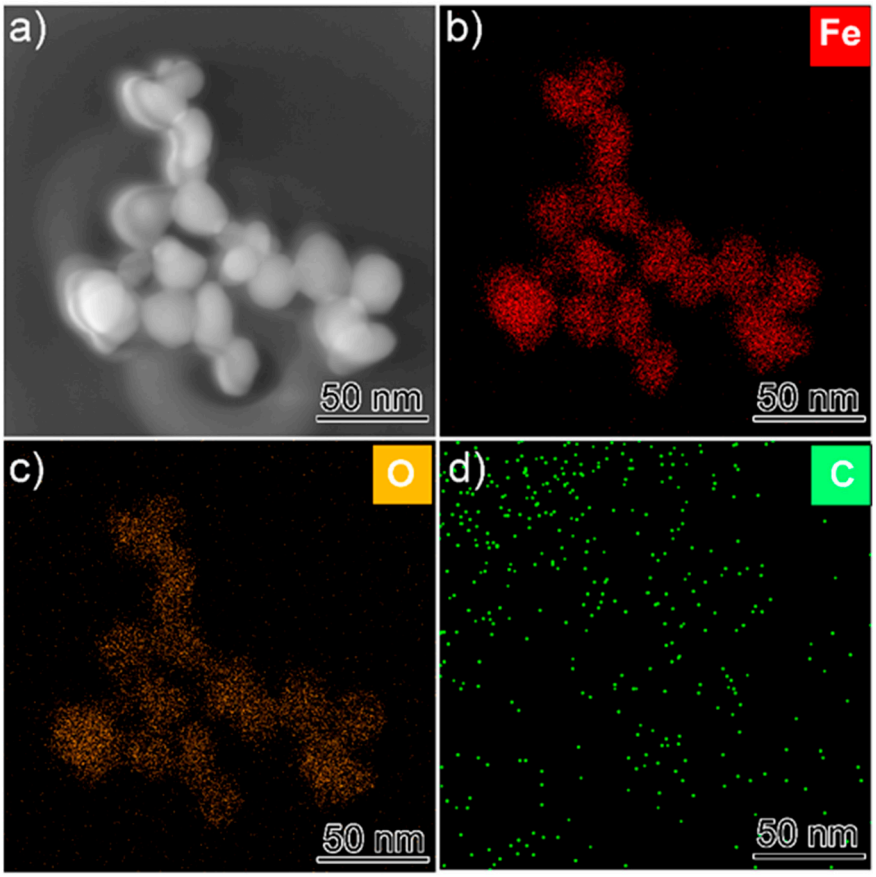

Figure 4. (**a**) STEM analysis of pure Fe_2O_3 nanoparticles, and (**b**–**d**) corresponding elemental mapping analysis of Fe, O, and C, respectively.

2.3. BET Analysis

Our next objective is to analyze the BET properties of Fe_2O_3 samples, both with and without a carbon layer, to evaluate their textural characteristics. The porosity and specific surface area of the photocatalysts were analyzed using nitrogen adsorption–desorption isotherms, conducted at 77 K. The specific surface area was calculated using the Brunauer–Emmett–Teller (BET) method, and the pore size distribution was obtained using the Barrett–Joyner–Halenda (BJH) method. The BET surface area of bare Fe_2O_3 nanoparticles and carbon-modified Fe_2O_3 nanoparticles was measured to be 19 m^2/g, and 45 m^2/g, respectively with an average pore diameter of both 16.3 nm and 5.8 nm, respectively as shown in Figure 5. The small and uniform particle size ensures a high surface area-to-volume ratio, which is beneficial for photocatalytic reactions as it provides more active sites for interaction with the reactants. The high porosity and specific surface area are crucial for enhancing the photocatalytic performance. The porous structure facilitates the diffusion of reactants and products to and from the active sites, improving the overall efficiency of the photocatalytic process.

2.4. Optical Analysis

Afterwards, we performed an investigation on the optical properties of pure Fe_2O_3 and Fe_2O_3@C nanoparticles. This was performed using UV-visible absorption spectroscopy, as shown in Figure 6a. The absorption intensity of both catalysts showed a noticeable rise as the wavelength decreased, which can be attributed to the unique nanocrystalline structure of the material [20]. The reason for the comparatively diminished UV-vis spectra of Fe_2O_3@C in contrast to Fe_2O_3 is the carbon content present in the Fe_2O_3/C sample. Carbon can absorb light, resulting in reduced light transmission through the sample and, consequently, diminished absorbance in the UV-vis spectra. Moreover, the carbon atom has

the potential to alter the electronic configuration of Fe_2O_3, thereby causing modifications to its optical characteristics, including light absorption and reflection. The confluence of these elements yields Fe_2O_3@C with diminished UV-vis spectra in comparison to Fe_2O_3. In previous studies, the absorption spectra of Fe_2O_3 nanoparticles have been divided into four distinct regions. These regions are categorized based on the varying transitions that occur within specific wavelength ranges. Region I span from 250 to 400 nm, region II ranges from 400 to 600 nm, region III covers 600 to 780 nm, and region IV extends from 750 to 900 nm. Unfortunately, the impediments to our measurements about the wavelength interval of 200–800 nm prevent us from obtaining precise information concerning region IV. Notably low absorption coefficients characterize Fe_2O_3 nanocrystals within the wavelength range of 600–900 nanometers. Absorption bands resulting from ligand-to-metal charge-transfer (LMCT) transitions are detected in region I. The absorption band detected in region II can be attributed to double excitation phenomena, which entail energy state transitions. These processes occur at wavelengths ranging from 485 to 550 nm. This absorption band may overlap with contributions from other transitions at 430 nm and the charge-transfer band tail. This transition is mainly responsible for the red color observed in hematite. In Region III, there is a ligand field transition happening at around 640 nm [32].

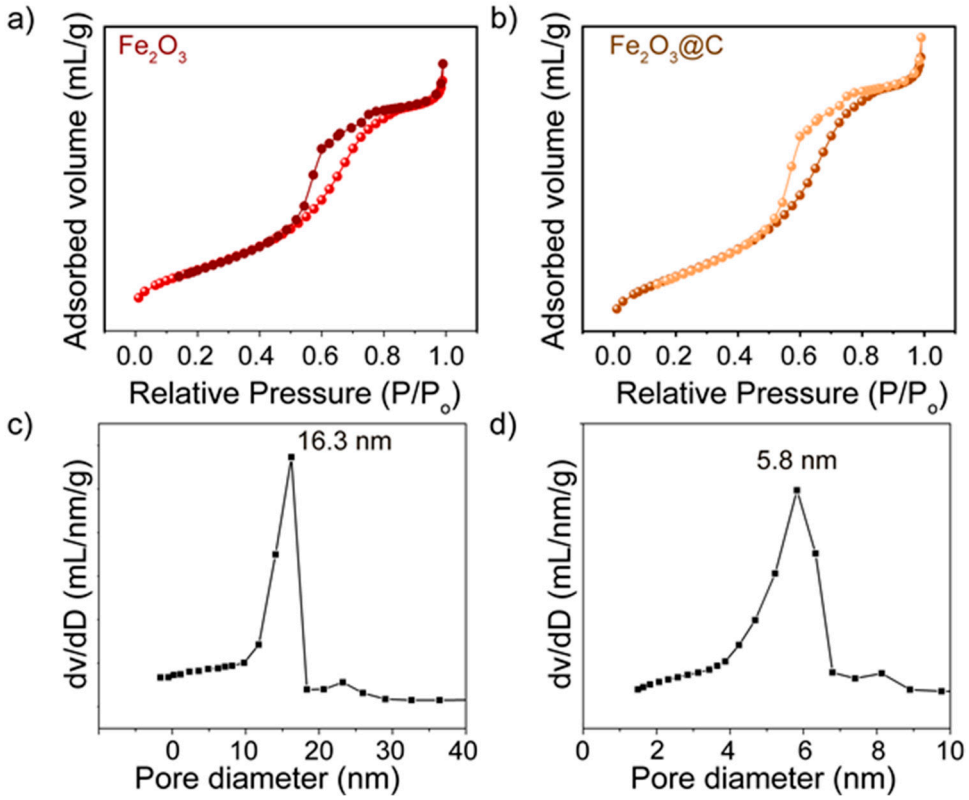

Figure 5. (**a**,**b**) BET analysis of Fe_2O_3 without and with a carbon layer, (**c**,**d**) corresponding pore size distribution.

The optical band gap of both pure Fe_2O_3 and Fe_2O_3@C nanoparticles can be determined using the following Equation (1):

$$\alpha = \frac{B(h\upsilon - Eg)^n}{h\upsilon} \quad (1)$$

where $h\upsilon$ represents the incident photon energy, α indicates the absorption coefficient, B is a material-dependent constant, and E_g represents the optical band gap. The value of n varies depending on the type of transition (i.e., direct bandgap or indirect bandgap) [3]. To determine E_g, the plot of $(\alpha h\upsilon)^{1/n}$ against $h\upsilon$, is constructed in Figure 6b and the

band gap can be calculated by projecting the linear segment of the absorption peak. The estimated direct band gap values for both Fe_2O_3 and Fe_2O_3@C are about 2.0 eV and 1.93 eV, respectively, as shown in Figure 6b. Some researchers have indicated Fe_2O_3 as an indirect band gap material [33] whereas others have pointed a direct band gap in Fe_2O_3 [34–36]. Moreover, other reports have shown that Fe_2O_3 contains both direct and indirect band gaps [1,2]. The indirect transition is due to spin-forbidden Fe^{3+} to 3d excitation, whereas the direct transition is related to the O^{2-} 2p to Fe^{3+} 3d charge transfer [34]. In our case, Fe_2O_3 has indirect transitions as evidenced by plotting $(\alpha h\upsilon)^{1/n}$ against $h\upsilon$ with n = 1/2 as shown in Figure 6b.

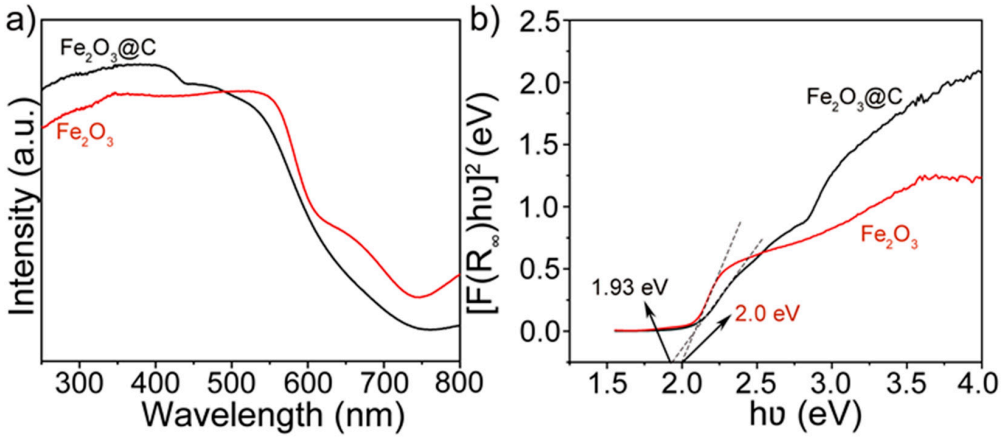

Figure 6. (**a**) UV-Vis absorption analysis, and (**b**) corresponding band gap of pure Fe_2O_3 and Fe_2O_3@C nanoparticles, respectively.

2.5. Methyl Orange (MO) Dye Degradation Analysis

2.5.1. Effect of pH and Irradiation Time

Using pure Fe_2O_3 and Fe_2O_3@C nanoparticles, the degradation of dye was studied in the presence and absence of H_2O_2 within a pH range of 3–8, as shown in Figures 7a and 7b, respectively. The results show that the degradation efficiency rises when the pH value decreases. As a result, when pH = 3 we achieve the highest dye degradation percentage. Furthermore, it was proven that the rate of dye degradation rose when H_2O_2 was added, as it can produce a greater number of hydroxyl free radicals (•OH) [3].

In a comparison of pure Fe_2O_3 and Fe_2O_3@C nanoparticles, we can see that utilizing the carbon-modified Fe_2O_3@C photocatalyst caused a superior dye degradation rate at all setting conditions. This anomaly can be explained by the fact that the Fe_2O_3@C photocatalyst had more amorphous and a smaller average crystallite size than the pure Fe_2O_3 photocatalyst. Furthermore, this leads to an augmentation in the surface area and enhancement in the efficiency of degradation.

As an anionic dye, MO orange responds to pH variations in distinct ways whereas Fe_2O_3 can take in hydrogen ions (H^+) from the solution when the pH is low. This causes it to become positively charged and results in the highest level of degradation. On the other hand, at higher pH values, Fe_2O_3 takes up hydroxide ions (OH^-), obtaining a negative charge and so leading to a reduced percentage of degradation [3,34]. Next, to assess the impact of irradiation time on the percentage of dye degradation using pure Fe_2O_3 and Fe_2O_3@C photocatalysts, experiments were conducted both in the absence and presence of H_2O_2, spanning a time range of 10–120 min, as illustrated in Figure 7c,d, respectively.

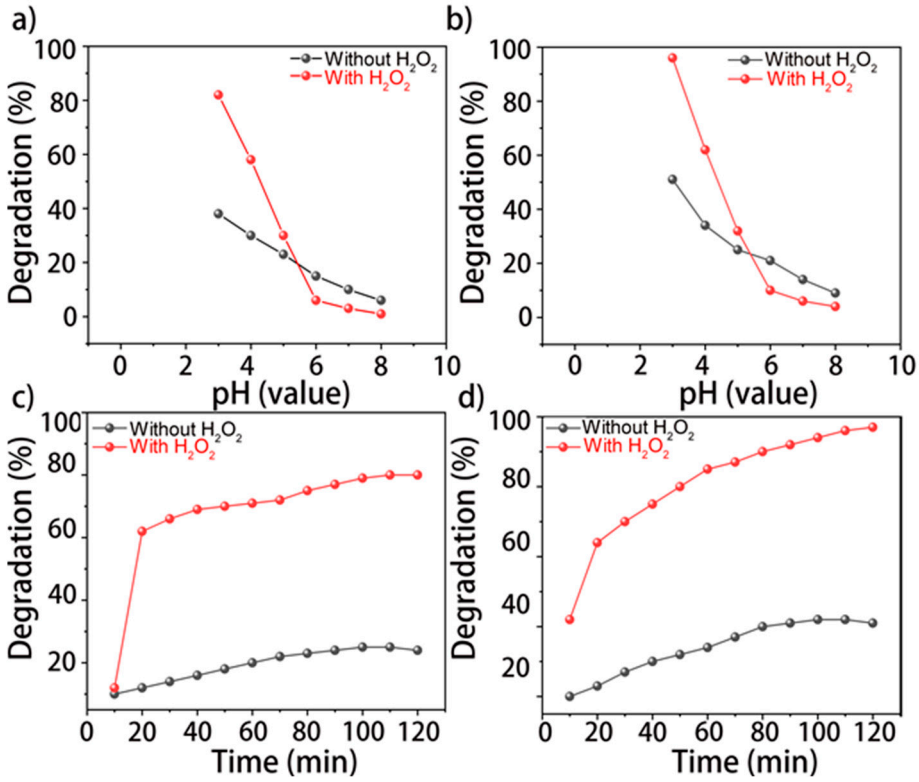

Figure 7. (**a**,**b**) Degradation (%) vs. pH value analysis, and (**c**,**d**) degradation (%) vs. time analysis of pure Fe_2O_3 and Fe_2O_3@C nanoparticles, respectively.

There was a noticeable increase in the percentage of dye degradation as the duration of irradiation was prolonged from 10 to 120 min. However, beyond 120 min, extending the irradiation time resulted in a nearly constant percentage degradation, indicative of saturation in the active sites. Therefore, we have identified 120 min as the optimal irradiation time for subsequent assessments. Furthermore, a significant increase in the proportion of dye degradation was observed when H_2O_2 was present, which can be attributed to its ability to produce additional •OH free radicals [3]. As shown in Figure 8a,b, the results obtained from the degradation of MO dye utilizing both pure Fe_2O_3 and Fe_2O_3@C nanoparticles in the presence and absence of H_2O_2 were consistent with the first-order kinetic model fitting as described in Equation (2) [31]:

$$ln\frac{Co}{Ce} = -Kt \quad (2)$$

where constant K (1/min) signifies a first-order reaction. To understand the photocatalytic degradation mechanism of methyl orange in the presence of the carbon-covered Fe_2O_3 photocatalyst, we analyzed the kinetic data obtained from our experiments, as shown in Figure 7c,d. This analysis helps in elucidating the reaction rate and the efficiency of the photocatalyst under different conditions. The degradation of methyl orange was analyzed using the pseudo-first-order kinetic model, which is commonly applied in photocatalytic degradation studies. A comparison of these results helps in understanding the influence of these parameters on photocatalytic efficiency. The kinetic data for the carbon-covered Fe_2O_3 were compared with those for uncovered Fe_2O_3. The carbon-covered photocatalyst exhibited significantly higher rate constants, demonstrating the effectiveness of the carbon coating in enhancing photocatalytic activity by improving charge separation and reducing recombination. The rate constants were compared with those reported in the literature for similar photocatalytic systems [3]. The comparison showed that carbon-covered Fe_2O_3 exhibited superior or comparable photocatalytic activity, highlighting the effectiveness of the carbon layer in enhancing the degradation kinetics. The kinetic analysis provides insights into the photocatalytic degradation mechanism. The pseudo-first-order behavior

suggests that the reaction is primarily controlled by the adsorption of methyl orange on the photocatalyst surface and subsequent photogenerated charge carrier reactions. Figure 8a,b depicts the analysis of ln (C_o/C_e) vs. time for pure Fe_2O_3 and Fe_2O_3@C photocatalysts, respectively.

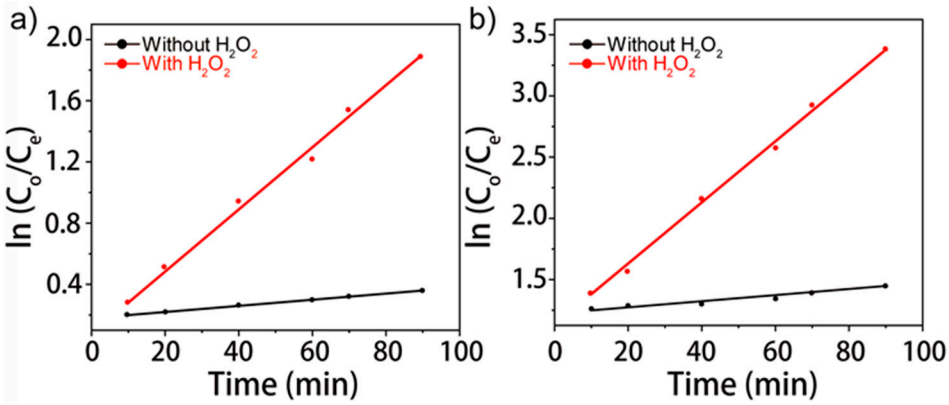

Figure 8. (**a**) Plot ln (C_o/C_e) vs. time analysis in the presence and absence of H_2O_2 for pure Fe_2O_3 and (**b**) Fe_2O_3@C photocatalysts.

2.5.2. Impact of Catalyst Dosage and Dye Concentration

The effect of pure Fe_2O_3 and carbon-modified Fe_2O_3@C nanoparticles dosage on the percentage degradation of dye is illustrated in Figure 9a,b. The percentage of degradation can be greatly influenced by the amount of catalyst; experiments were carried out using different concentrations of both nanoparticles, ranging from 10 to 110 mg. The maximum degradation efficiency was attained when 30 mg of Fe_2O_3@C nanoparticles with a carbon-modified layer were used. Moreover, a higher concentration of Fe_2O_3 nanoparticles led to a higher percentage of dye degradation, especially when H_2O_2 was present since it helped produce more •OH free radicals. The increase in the number of nanoparticles enhances the number of active sites on their surface, increasing the number of free radicals that can expedite dye degradation [7,36].

Increasing the quantity of Fe_2O_3 nanoparticles beyond a certain threshold (30 mg) diminishes the catalytic degradation of dye due to the accumulation of nanoparticles, resulting in a decrease in surface area and active sites. Thus, it has been determined that the most effective amount of catalyst for future evaluations is 30 mg. Furthermore, the reduction in photocatalytic activity occurs because the MO dye solution undergoes a phase transition from homogeneous to turbid. This transition impedes the penetration of UV-vis light irradiation into the solution. Thus, the percentage of dye degradation is diminished due to the scattering of UV irradiation.

Subsequently, an analysis was conducted to assess the photocatalytic dye degradation using both pure Fe_2O_3 and carbon-modified Fe_2O_3@C nanoparticles and different dye concentrations in presentence and absence of hydrogen peroxide, as shown in Figures 9c and 9d, respectively. This analysis was performed at varying concentrations of MO dye, ranging from 10 to 20 mg/L. The results indicate an inverse relationship between dye concentration and degradation efficiency. The decrease in UV-vis light penetration through the hematite surface can be attributed to the increased concentration of dye adsorbed on the surface of hematite nanoparticles. The generation of e^-/h^+ pairs on the surface of Fe_2O_3 and the subsequent formation of •OH free radicals are responsible for reducing the degradation of MO [34]. Furthermore, it was observed that the proportion of dye degradation increased when H_2O_2 was present, due to its ability to generate extra •OH free radicals.

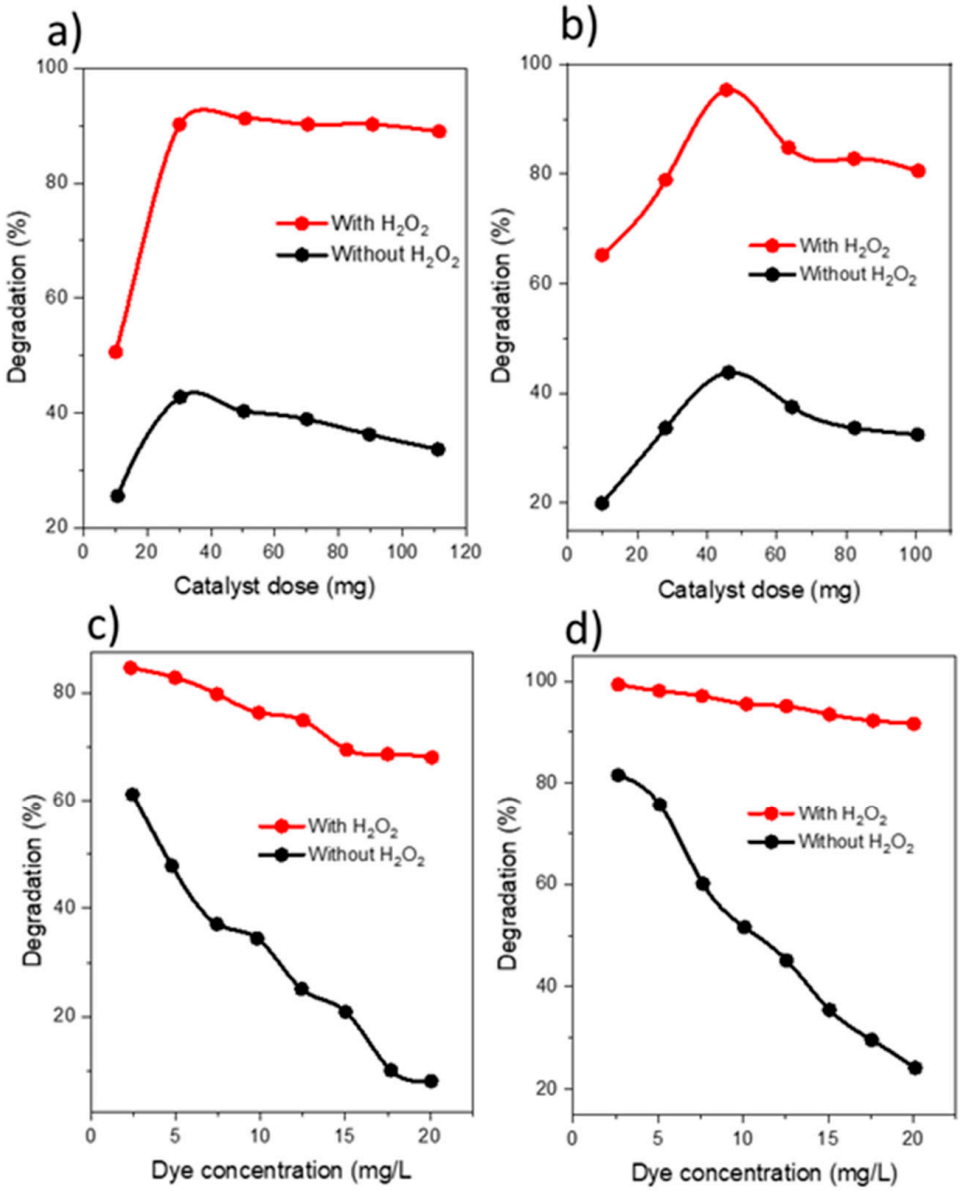

Figure 9. (**a**,**b**) Degradation (%) vs. dose of catalyst analysis and (**c**,**d**) degradation (%) vs. concentration of dye analysis of pure Fe_2O_3 and Fe_2O_3@C nanoparticles, respectively.

2.5.3. Trapping Species Analysis

To elucidate the mechanism of methyl orange oxidation during the photocatalytic process, we propose to use scavengers for different reactive species such as isopropanol (IPA), ethylenediaminetetraacetic acid disodium salt (EDTA-2Na) and p-benzoquinone (p-BQ) as efficient scavengers for hydroxyl radical (·OH), and superoxide radical ($\cdot O_2^-$), respectively to assess their impact on the degradation efficiency. This approach will help to identify the primary reactive species involved in the oxidation mechanism. As shown in Figure 10, when we added p-BQ, the degradation rate of MO was decreased. Hence, we conclude that $\cdot O_2^-$ was the main reactive species for the degradation of MO by C@Fe_2O_3.

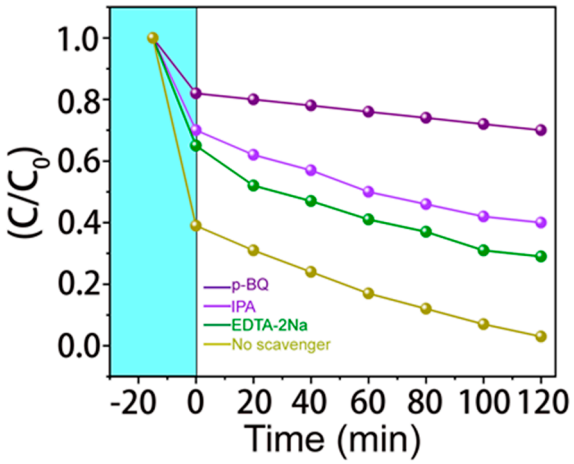

Figure 10. Radical scavenging analysis to determine the reaction mechanism.

2.5.4. Impact of Renewal and Recyclability

Four additional cycles were required to regenerate the Fe_2O_3 nanoparticles that were generated. After each cycle, the Fe_2O_3 nanoparticles were carefully rinsed with hot distilled water to renew the hematite photocatalyst, producing a catalyst that was nearly identical to the one used for the next cycle. In addition, it was observed in Figure 11a,b that the Fe_2O_3@C nanoparticles maintained their photocatalytic efficiency, with only a slight decrease in the percentage degradation value compared to pure Fe_2O_3 nanoparticles without carbon layer in the presence and absence of hydrogen peroxide.

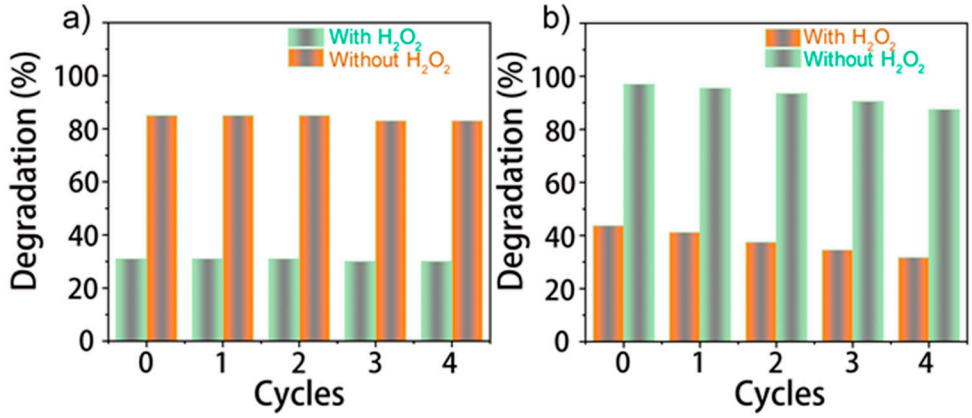

Figure 11. Plot of Degradation (%) vs. Cycles of (**a**) pure Fe_2O_3 and (**b**) Fe_2O_3@C nanoparticles.

2.5.5. Mechanism in Photocatalytic Degradation

To provide a comprehensive discussion on the role of the conductive carbon layer, and H_2O_2 in the photocatalytic degradation of methyl orange, we also consider the photo-Fenton-like process and its impact on the reaction mechanism [21–25]. When H_2O_2 is added to the photocatalytic system, it can enhance the degradation of organic pollutants by generating additional hydroxyl radicals (•OH) via a photo-Fenton-like reaction using H_2O_2 and Fe(II/III) redox in the presence of light. These reactions show that the presence of H_2O_2 can lead to the continuous generation of hydroxyl radicals, significantly enhancing the oxidation of methyl orange. In our study, we observed an enhanced degradation rate of methyl orange when H_2O_2 was added to the photocatalytic system. This indicates the involvement of a photo-Fenton-like process, contributing to the generation of additional hydroxyl radicals.

Figure 12 depicts the thought of the MO photocatalytic degradation mechanism using pure Fe_2O_3 and carbon-modified Fe_2O_3@C nanoparticles. Both activated the electron/hole pairs on the surface when exposed to UV-vis light radiation. Carbon-modified Fe_2O_3

nanoparticles degrade methyl orange dye more effectively than bare Fe_2O_3 nanoparticles. The carbon layer works as a cocatalyst, improving charge separation and light energy utilization while protecting against photo-corrosion and aggregation. It also increases surface area and provides new adsorption sites, which improves dye adsorption and overall degradation efficiency. Extending light absorption into the visible range allows for more effective use of the solar spectrum. Electron transfer from photoexcited nanoparticles to dye molecules occurs quickly, which accelerates degradation kinetics. The thickness and composition of the carbon layer are tailored to optimize photocatalytic activity for specific applications, increasing dye degradation efficiency. Afterward, these generated electron/hole pairs interact with water molecules to produce •OH free radicals, which can degrade the dye into safe byproducts such as water and carbon dioxide. The enhanced degradation can be attributed to the increased production of hydroxyl radicals through Fenton reaction involving H_2O_2 and Fe ions. This suggests that both the photocatalytic process and the photo-Fenton-like process contribute synergistically to the degradation of methyl orange [21–25]. The concentration of H_2O_2 and the initial pH of the solution were optimized to maximize the degradation efficiency. Higher concentrations of H_2O_2 up to an optimal level improved the degradation rate, beyond which the rate plateaued or decreased due to the scavenging effect of excess H_2O_2.

$$Fe_2O_3 + h\nu \rightarrow h^+ + e^-$$
$$H_2O \rightarrow H^+ + OH^-$$
$$h^+ + OH^- \rightarrow {}^\bullet OH$$
$$e^- + O_2 \rightarrow O_2^{-\bullet}$$
$$O_2^{-\bullet} + H^+ \rightarrow HOO^\bullet$$
$$2HOO^\bullet \rightarrow H_2O_2 + O_2$$
$$H_2O_2 + h\nu \rightarrow 2OH^\bullet$$

Dye Degradation:
$$^\bullet OH + RH \rightarrow R^\bullet + H_2O$$
$$H_2O_2 + h\nu\,(UV) \rightarrow 2OH^\bullet$$

Figure 12. The photocatalytic degradation mechanism of MO dye.

3. Experimental Section

3.1. Chemicals Reagents

All reagents utilized were of analytical grade and required no additional purification. The following chemicals were procured from Sinopharm Chemical Reagent Co., Ltd. (Shanghai, China). Iron trichloride hexahydrate ($FeCl_3{\cdot}6H_2O$, 99%), terephthalic acid (H_2BDC), N-dimethylformamide (DMF), dicyandiamide (DCDA), and ethanol anhydrous (C_2H_6O). MO dye was purchased from Sigma Aldrich (Saint Louis, MO, USA). Deionized (DI) water was utilized in every experiment.

3.2. Synthesis of Fe_2O_3 Nanoparticles Modified with Carbon Layer

Terephthalic acid (H_2BDC) acts as an organic ligand to form a metal–organic framework (MOF) precursor with iron ions. DMF is used as a solvent to dissolve the terephthalic acid and facilitate the formation of the MOF. It also acts as a carbon source upon decomposition. DMF decomposition under thermal treatment. Ethanol is used as a solvent to wash and purify the synthesized nanoparticles, ensuring the removal of unreacted precursors and by-products. Ethanol does not participate in the chemical reaction but aids in purification. The method of using MOF precursors for synthesizing Fe_2O_3 nanoparticles was chosen due to the controllable structure and high surface area of MOFs, which are beneficial for creating a uniform and well-dispersed nanoparticle. The choice of H_2BDC and DMF was influenced by their common use in MOF synthesis, providing a reliable pathway to form the desired Fe-BDC MOF precursor.

The synthesis of Fe_2O_3 nanoparticles modified with a carbon layer (Fe_2O_3@C) was performed by dissolving $FeCl_3{\cdot}6H_2O$ (1.0 g) and H_2BDC (50 mg) in a mixture of 30 mL ethanol (EtOH) and 30 mL DMF within an autoclave of total volume (100 mL). After stirring

for 25 min to make a clear solution, the Teflon-lined stainless-steel autoclave was sealed and heated at 120 °C for 5.0 h. The resulting dark brown mixture was subsequently subjected to centrifugation and washed with DMF and ethanol several times to eliminate contaminants. Finally, Fe_2O_3@C nanoparticles are obtained by drying at 80 °C for 7 h in a vacuum oven.

3.3. Synthesis of Pure Fe_2O_3 Nanoparticles

The synthesis of pure Fe_2O_3 was achieved by a hydrothermal technique as shown in Figure 13a. Specifically, a solution was prepared by dissolving 1.0 g of $FeCl_3 \cdot 6H_2O$ in 60 mL of ethanol solution in an autoclave with a total volume of 100 mL. The solution was agitated for a few minutes until it turned clear. Afterwards, a solution of sodium hydroxide (0.12 g) in water was gradually introduced to the ferric chloride solution. The resulting reagents were agitated constantly at ambient temperature for a brief duration to obtain a yellow suspension, which was subsequently transferred to an autoclave. The autoclave was hermetically sealed and subjected to hydrothermal treatment at a temperature of 90 °C for five hours. The resultant yellow colloidal solution was subjected to centrifugation to eliminate any contaminants and subsequently rinsed multiple times with deionized water and ethanol. The produced yellow solid underwent drying at a temperature of 80 °C overnight. As illustrated in Figure 13b, the carbon-free pure phase of Fe_2O_3 was effectively achieved by subjecting the above yellow precipitate to heat treatment at a temperature of 300 °C for approximately two hours. The schematic diagrams below illustrate the synthesis processes of Fe_2O_3 nanoparticles, both with and without the incorporation of a carbon layer.

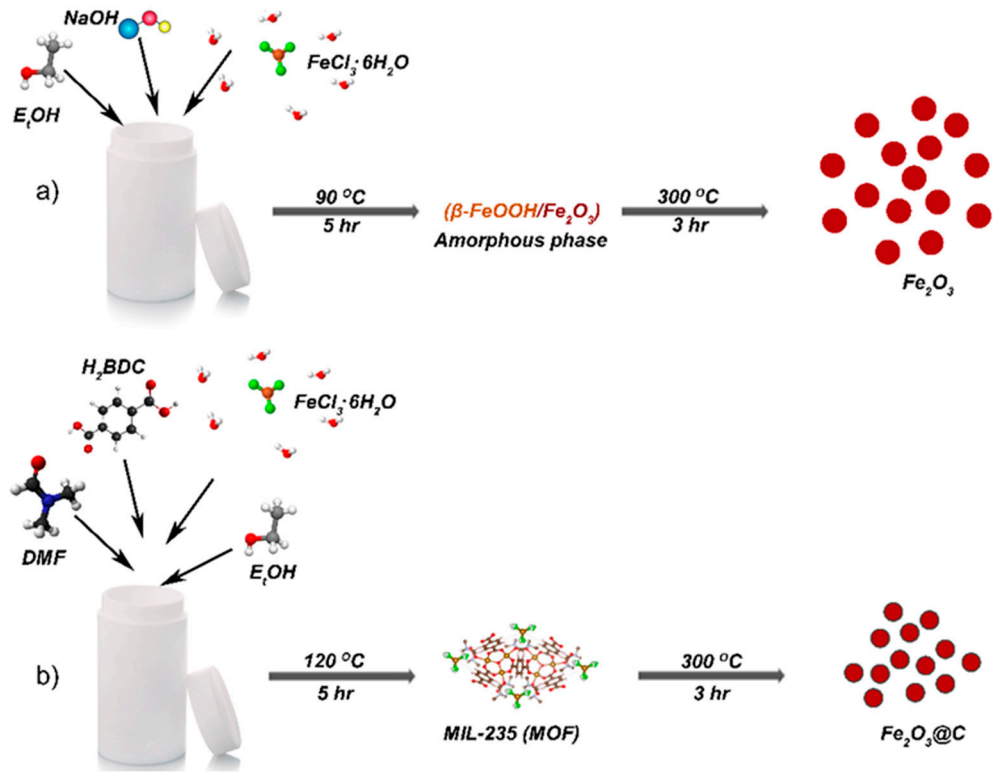

Figure 13. (**a**) Schematic illustration of Fe_2O_3 nanoparticles without carbon layer, (**b**) corresponding Fe_2O_3 nanoparticles with carbon layer.

3.4. Methyl Orange (MO) Dye Degradation via Photocatalysis

The effectiveness of the prepared pure Fe_2O_3 and carbon-modified Fe_2O_3@C in degrading MO dye under UV irradiation was investigated. In each photocatalytic trial, a mixture comprising 30 mL of 15 mg/L MO orange solution and 0.03 g of either pure Fe_2O_3 or carbon-modified Fe_2O_3@C nanoparticles was stirred in darkness for 60 min before expo-

sure to light irradiation. Afterward, the nanoparticles of photocatalysts were separated by spinning them at a speed of 5000 revolutions per minute using a centrifuge. The amount of MO dye in the liquid that passed through the filter was measured using UV–vis spectroscopy within the wavelength where the dye absorbs the maximum light (i.e., 465 nm). Repetition of these procedures was achieved by adding 2.0 mL of a 2.0 M H_2O_2 solution. Experiments were conducted to study the degradation of MO dye in different aqueous environments including pure Fe_2O_3 and carbon-modified Fe_2O_3@C nanoparticles at various dosages ranging from 0.0125 to 0.20 g, pH levels from 3 to 8, irradiation durations from 10 to 120 min, and MO dye concentrations from 5 to 30 mg/L). The degree of photocatalytic degradation (D%) was computed using Equation (3).

$$D\% = \frac{Co - Ce}{Co} * 100 \quad (3)$$

The initial concentration of the MO dye pigment is denoted as C_o (mg/L), whereas the equilibrium concentration is represented by C_e (mg/L).

3.5. Physicochemical Measurements

The powder X-ray diffraction (XRD) analysis was conducted using a Malvern PANalytical X'pert Pro MPD diffractometer (ICN2, Barcelona, Spain) with Ni-filtered Cu Kα radiation (wavelength, λ = 1.5406 Å). The Fourier-transform infrared spectra were utilized to analyze the surface functional groups of the pure Fe_2O_3 and carbon-modified Fe_2O_3@C catalysts. The KBR powder technique was utilized on the Bruker Vertex 70 infrared spectrophotometer (Billerica, MA, USA). An examination of the microstructure and microcrystalline morphology was performed utilizing techniques including TEM/HRTEM (Fei Tecnai G2 F30 S-Twin, FEI, Los Alamos National Laboratory, Los Alamos, NW, USA) integrated with an EDX detector (OXFORD MAX-80, Oxford, UK). The SEM model (JEOL-JSM-7800F, Hitache High Technology, Tokyo, Japan) was used to determine the surface morphology and size of the photocatalysts. The optical parameters of the photocatalytic material were analyzed using a U-4100 UV-vis spectrometer, namely the Hitachi model. The content of carbon in Fe_2O_3@C and Fe_2O_3 was obtained with the help of elemental analysis (Vario MACRO Cube, BRS, Beersel, Belgium).

4. Conclusions

In this study, pure Fe_2O_3 and carbon-modified Fe_2O_3@C nanoparticles were synthesized via a simple solvothermal route. The XRD, FTIR, UV-vis TEM, and HRTEM were used to characterize the synthesized photocatalysts. The Fe_2O_3 nanoparticles with and without carbon layer had an average crystallite size of about 50 nm and 20 nm, respectively. Additionally, under visible light irradiation, the Fe_2O_3@C photocatalyst showed effective photocatalytic activity to degrade MO dye, both in the presence and absence of H_2O_2. The results indicate that in the presence of H_2O_2, the best conditions were found to be a pH of 3, an irradiation time of 120 min, and a catalyst dosage of 30 mg. The degradation efficiency reached 77% and 97% for the pure Fe_2O_3 and Fe_2O_3@C photocatalysts, respectively. The results demonstrated the impact of the carbon modification layer on the photocatalytic behavior of Fe_2O_3 and the reduced electron–hole recombination rate.

Author Contributions: M.Q.: conceptualization, methodology, validation, investigation, data curation, writing—original draft preparation, resources; X.L.: software, visualization; X.C.: formal analysis, M.A.G.: conceptualization, funding acquisition, writing—review and editing, project administration. All authors have read and agreed to the published version of the manuscript.

Funding: This work was supported by the Qilu Institute of Technology, Zhangqiu Jinan China. The authors would also express their sincere gratitude to the Researchers Supporting Program, Project number (RSP2024R518), King Saud University, Riyadh, Saudi Arabia.

Data Availability Statement: Data will be available at a reasonable request from the corresponding author.

Acknowledgments: This work was supported by the Qilu Institute of Technology, Zhangqiu Jinan China. The authors would like to express their sincere gratitude to the Researchers Supporting Program, project number (RSP2024R518), King Saud University, Riyadh, Saudi Arabia.

Conflicts of Interest: The funders had no role in the design of the study; in the collection, analyses, or interpretation of data; in the writing of the manuscript; or in the decision to publish the results.

References

1. El Amri, A.; Kadiri, L.; Hsissou, R.; Lebkiri, A.; Wardighi, Z.; Rifi, E.H.; Lebkiri, A. Investigation of Typha Latifolia (TL) as Potential Biosorbent for Removal of the Methyl Orange Anionic Dye in the Aqueous Solution. Kinetic and DFT Approaches. *J. Mol. Struct.* **2023**, *1272*, 134098. [CrossRef]
2. Gautam, I.; Grady, T.; Fernando, H. Degradation of the Dye Methyl Orange Using Cow and Goat Milk Iron Nanoparticles. *Green Chem. Lett. Rev.* **2023**, *16*, 2174818. [CrossRef]
3. Shah, R.K. Efficient Photocatalytic Degradation of Methyl Orange Dye Using Facilely Synthesized α-Fe_2O_3 Nanoparticles. *Arab. J. Chem.* **2023**, *16*, 104444. [CrossRef]
4. Hussain, S.; Kamran, M.; Khan, S.A.; Shaheen, K.; Shah, Z.; Suo, H.; Khan, Q.; Shah, A.B.; Rehman, W.U.; Al-Ghamdi, Y.O.; et al. Adsorption, Kinetics and Thermodynamics Studies of Methyl Orange Dye Sequestration through Chitosan Composites Films. *Int. J. Biol. Macromol.* **2021**, *168*, 383–394. [CrossRef]
5. Jayakumar, P.; Palani, S.; Nallathambi, M.; Kuppusamy, K. Evaluation of $MnWO_4$ Nanomaterial for Enhanced Photocatalytic Degradation Activity over Methyl Orange Dye. *Lett. Appl. NanoBioScience* **2024**, *13*, 1–16. [CrossRef]
6. Kumar, P.; Thakur, N.; Kumar, K.; Jeet, K. Photodegradation of Methyl Orange Dye by Using Azadirachta Indica and Chemically Mediated Synthesized Cobalt Doped α-Fe_2O_3 NPs through Co-Precipitation Method. *Mater. Today Proc.* **2023**. [CrossRef]
7. Wang, T.; Huang, M.; Liu, X.; Zhang, Z.; Liu, Y.; Tang, W.; Bao, S.; Fang, T. Facile One-Step Hydrothermal Synthesis of α-Fe_2O_3/g-C_3N_4 Composites for the Synergistic Adsorption and Photodegradation of Dyes. *RSC Adv.* **2019**, *9*, 29109–29119. [CrossRef]
8. Nasirian, M.; Bustillo-Lecompte, C.F.; Mehrvar, M. Photocatalytic Efficiency of Fe_2O_3/TiO_2 for the Degradation of Typical Dyes in Textile Industries: Effects of Calcination Temperature and UV-Assisted Thermal Synthesis. *J. Environ. Manag.* **2017**, *196*, 487–498. [CrossRef]
9. Othman, N.W.; Radde, H.; Puah, P.Y.; Ling, Y.S.; Moh, P.Y. Enhancing Photocatalytic Activity of Titanium Dioxide through Incorporation of MIL-53(Fe) toward Degradation of Organic Dye. *J. Chin. Chem. Soc.* **2019**, *66*, 81–88. [CrossRef]
10. Khalaji, A.D. Spherical α-Fe_2O_3 Nanoparticles: Synthesis and Characterization and Its Photocatalytic Degradation of Methyl Orange and Methylene Blue. *Phys. Chem. Res.* **2022**, *10*, 473–483. [CrossRef]
11. Vijayakumar, T.P.; Benoy, M.D.; Duraimurugan, J.; Kumar, G.S.; Shkir, M.; Maadeswaran, P.; Srinivasan, R.; Prabhu, S.; Ramesh, R.; Haseena, S. Investigation on Photocatalytic Activity of G-C_3N_4 Decorated α-Fe_2O_3 Nanostructure Synthesized by Hydrothermal Method for the Visible-Light Assisted Degradation of Organic Pollutant. *Diam. Relat. Mater.* **2022**, *125*, 109021. [CrossRef]
12. Weldegebrieal, G.K.; Sibhatu, A.K. Photocatalytic Activity of Biosynthesized α-Fe_2O_3 Nanoparticles for the Degradation of Methylene Blue and Methyl Orange Dyes. *Optik* **2021**, *241*, 167226. [CrossRef]
13. Al-Mamun, M.R.; Iqbal Rokon, M.Z.; Rahim, M.A.; Hossain, M.I.; Islam, M.S.; Ali, M.R.; Bacchu, M.S.; Waizumi, H.; Komeda, T.; Hossain Khan, M.Z. Enhanced Photocatalytic Activity of Cu and Ni-Doped ZnO Nanostructures: A Comparative Study of Methyl Orange Dye Degradation in Aqueous Solution. *Heliyon* **2023**, *9*, e16506. [CrossRef] [PubMed]
14. Suryavanshi, R.D.; Mohite, S.V.; Bagade, A.A.; Rajpure, K.Y. Photoelectrocatalytic Activity of Spray Deposited Fe_2O_3/ZnO Photoelectrode for Degradation of Salicylic Acid and Methyl Orange Dye under Solar Radiation. *Mater. Sci. Eng. B* **2019**, *248*, 114386. [CrossRef]
15. Panda, N.; Sahoo, H.; Mohapatra, S. Decolourization of Methyl Orange Using Fenton-like Mesoporous Fe_2O_3-SiO_2 Composite. *J. Hazard. Mater.* **2011**, *185*, 359–365. [CrossRef] [PubMed]
16. Singh Rathore, B.; Pal Singh Chauhan, N.; Panneerselvam, P.; Jadoun, S.; Barani, M.; Ameta, S.C.; Ameta, R. Synthesis and Characterization of Ch-PANI-Fe_2O_3 Nanocomposite and Its Water Remediation Applications. *Water* **2022**, *14*, 3615. [CrossRef]
17. Yaou Balarabe, B.; Illiassou Oumarou, M.N.; Koroney, A.S.; Adjama, I.; Ibrahim Baraze, A.R. Photo-Oxidation of Organic Dye by Fe_2O_3 Nanoparticles: Catalyst, Electron Acceptor, and Polyurethane Membrane (PU-Fe_2O_3) Effects. *J. Nanotechnol.* **2023**, *2023*, 1292762. [CrossRef]
18. Nasri, A.; Nezafat, Z.; Jaleh, B.; Orooji, Y.; Varma, R.S. Laser-Assisted Preparation of C_3N_4/Fe_2O_3/Au Nanocomposite: A Magnetic Reusable Catalyst for Pollutant Degradation. *Clean Technol. Environ. Policy* **2021**, *23*, 1797–1806. [CrossRef]
19. Khurram, R.; Wang, Z.; Ehsan, M.F.; Peng, S.; Shafiq, M.; Khan, B. Synthesis and Characterization of an α-Fe_2O_3/ZnTe Heterostructure for Photocatalytic Degradation of Congo Red, Methyl Orange and Methylene Blue. *RSC Adv.* **2020**, *10*, 44997–45007. [CrossRef]
20. Qasim, M.; Liu, M.; Guo, L. Electron Transfer via a Carbon Channel for Efficient Z-Scheme Solar Hydrogen Production. *Int. J. Hydrogen Energy* **2021**, *46*, 28098–28109. [CrossRef]
21. Hussain, S.; Aneggi, E.; Goi, D. Catalytic Activity of Metals in Heterogeneous Fenton-like Oxidation of Wastewater Contaminants: A Review. *Environ. Chem. Lett.* **2021**, *19*, 2405–2424. [CrossRef]

22. Zhang, L.; Ding, R.; Mao, C.; Guo, T.; Xue, X.; Bi, L.; Yan, B.; Zhang, Z. Highly Efficient Heterogeneous Photo-Fenton-like Catalyst of e-Fe_2O_3/SiO_2/Attapulgite with Rich Oxygen Vacancies for Photocatalytic Degradation of Organic Pollutants. *ChemistrySelect* **2022**, *7*, e202201382. [CrossRef]
23. Li, J.; You, J.; Wang, Z.; Zhao, Y.; Xu, J.; Li, X.; Zhang, H. Application of α-Fe_2O_3-Based Heterogeneous Photo-Fenton Catalyst in Wastewater Treatment: A Review of Recent Advances. *J. Environ. Chem. Eng.* **2022**, *10*, 108329. [CrossRef]
24. Magomedova, A.; Isaev, A.; Orudzhev, F.; Sobola, D.; Murtazali, R.; Rabadanova, A.; Shabanov, N.S.; Zhu, M.; Emirov, R.; Gadzhimagomedov, S.; et al. Magnetically Separable Mixed-Phase α/γ-Fe_2O_3 Catalyst for Photo-Fenton-like Oxidation of Rhodamine B. *Catalysts* **2023**, *13*, 872. [CrossRef]
25. SalehHudin, H.S.; Mohamad, E.N.; Mahadi, W.N.L.; Muhammad Afifi, A. Multiple-Jet Electrospinning Methods for Nanofiber Processing: A Review. *Mater. Manuf. Process.* **2018**, *33*, 479–498. [CrossRef]
26. Kaushik, J.; Twinkle, N.; Tisha, N.; Nisha, N.; Baig, A.; Sonal, N.; Dubey, P.; Sonkar, S.K. Photoactive Fe_3O_4@Fe_2O_3 Synthesized from Industrial Iron Oxide Dust for Fenton-Free Degradation of Multiple Organic Dyes. *Ind. Eng. Chem. Res.* **2023**, *62*, 10487–10497. [CrossRef]
27. Qasim, M.; Xue, F.; Liu, M.; Guo, L. Phase-Transition-Induced One-Dimensional Amorphous α-Fe_2O_3/β-FeOOH Homojunction for Efficient Photocatalytic Water Oxidation. *J. Photonics Energy* **2019**, *9*, 026501. [CrossRef]
28. Zhou, X.; Liu, H.; Liu, S.; Zhang, L.; Wang, T.; Wang, C.; Su, D. Constructing Efficient α-Fe_2O_3/g-C_3N_4/HNTs-Loaded Heterojunction Photocatalysts for Photocatalytic Oxidative Desulfurization: Influencing Factors, Kinetics, and Mechanism. *Fuel* **2023**, *332*, 126147. [CrossRef]
29. Mukhtar, F.; Munawar, T.; Nadeem, M.S.; Hasan, M.; Hussain, F.; Nawaz, M.A.; Iqbal, F. Multi Metal Oxide NiO-Fe_2O_3-CdO Nanocomposite-Synthesis, Photocatalytic and Antibacterial Properties. *Appl. Phys. A Mater. Sci. Process* **2020**, *126*, 588. [CrossRef]
30. Omran, M.; Fabritius, T.; Elmahdy, A.M.; Abdel-Khalek, N.A.; El-Aref, M.; Elmanawi, A.E.H. XPS and FTIR Spectroscopic Study on Microwave Treated High Phosphorus Iron Ore. *Appl. Surf. Sci.* **2015**, *345*, 127–140. [CrossRef]
31. Qasim, M.; Liu, M.; Guo, L. Z-Scheme P-Doped-g-C_3N_4/Fe2P/Red-P Ternary Composite Enables Efficient Two-Electron Photocatalytic Pure Water Splitting. *Catal. Today* **2023**, *409*, 119–127. [CrossRef]
32. Mallick, P.; Dash, B.N. X-ray Diffraction and UV-Visible Characterizations of α-Fe_2O_3 Nanoparticles Annealed at Different Temperature. *Nanosci. Nanotechnol.* **2013**, *3*, 130–134.
33. Tahir, M.; Fakhar-e-Alam, M.; Atif, M.; Mustafa, G.; Ali, Z. Investigation of Optical, Electrical and Magnetic Properties of Hematite α-Fe_2O_3 Nanoparticles via Sol-Gel and Co-Precipitation Method. *J. King Saud. Univ. Sci.* **2023**, *35*, 102695. [CrossRef]
34. Hmamouchi, S.; El Yacoubi, A.; El Idrissi, B.C. Using Egg Ovalbumin to Synthesize Pure α-Fe_2O_3 and Cobalt Doped α-Fe_2O_3: Structural, Morphological, Optical and Photocatalytic Properties. *Heliyon* **2022**, *8*, e08953. [CrossRef] [PubMed]
35. Hegazey, R.M.; Abdelrahman, E.A.; Kotp, Y.H.; Hameed, A.M.; Subaihi, A. Facile Fabrication of Hematite Nanoparticles from Egyptian Insecticide Cans for Efficient Photocatalytic Degradation of Rhodamine B Dye. *J. Mater. Res. Technol.* **2020**, *9*, 1652–1661. [CrossRef]
36. Wang, F.; Song, L.X.; Teng, Y.; Xia, J.; Xu, Z.Y.; Wang, W.P. Synthesis, Structure, Magnetism and Photocatalysis of α-Fe_2O_3 Nanosnowflakes. *RSC Adv.* **2019**, *9*, 35372–35383. [CrossRef]